



Dissimilar Metal Joining of 304 Stainless Steel to SMA490BW Steel Using the Filler Metal Powders with a High-Entropy Design

Dejia Liu^{1,2} · Rui Guo¹ · Yong Hu¹ · Mingxue Shen¹ · Yanchuan Tang¹ · Longzhi Zhao¹ · Deying Li¹ · Xiangjie Wang³

Received: 15 May 2019 / Accepted: 25 July 2019 / Published online: 1 August 2019
© The Korean Institute of Metals and Materials 2019

Abstract

High-entropy alloys having excellent properties are particularly suitable for the application as the filler metals in welding. In the present study, multi-component mixed powders of FeCoCrNiMn and CrFeNi_{2.4}Al_{0.6}, based on a high-entropy design, as well as the comparative 316L stainless steel powders, were used as the filler metals, to achieve the dissimilar welding between 304 stainless steel and SMA490BW steel by laser deposition welding. By comparative analysis of the microstructure and mechanical properties of three types of joints, the feasibility and weld-ability of the filler metal powders based on a high-entropy design were studied. It was found that the melting of base metal (BM) and weld metal dilution had an impact on the set high-entropy component in the weld zone. And high-entropy structures were achieved in the weld zone by using the powders of CrFeNi_{2.4}Al_{0.6}. Compared to the BM of SMA490BW steel, three types of joints presented a higher notched tensile strength and had a better corrosion resistance. The joint welded using the powders of CrFeNi_{2.4}Al_{0.6} had the lowest hardness value in the weld zone, in which the joint was fractured during the notched tensile tests. The other two joints fractured near the notch in the SMA490BW steel side. Transgranular fracture and a typical dimple fracture were observed in the fractured joints.

Keywords High-entropy filler metals · Laser deposition welding · Microstructure · Hardness · Notched tensile tests

1 Introduction

High-entropy alloys (HEAs) are defined as alloys with equal or nearly equal quantities of five or more principal elements [1, 2]. Owing to the excellent properties, including high strength/hardness, good corrosion and oxidation resistance,

good structural stability, HEAs have broad application prospects, and have attracted widespread attention [1–4]. The microstructure, mechanical properties and corrosion resistance of HEAs are widely studied in many previous studies [5–9]. By modifying the chemical composition and crystal structures, an excellent combination of high strength and good fracture toughness can be obtained in HEAs [10–12]. Many scholars have used laser beam welding [13–16], friction stir welding [17–21], and gas-tungsten-arc-welding [21–24], to explore the weld-ability of HEAs as structural materials. However, it should be pointed out that, the high strength and good fracture toughness of HEAs are particularly suitable to apply in welding, especially served as the filler metal during welding process [1, 25, 26]. Therefore, it is meaningful to evaluate the microstructures and mechanical properties of the welded joints using the filler metal of HEAs, so as to improve the strength and toughness of the joints and expand the application of HEAs served as the filler metal during the welding process.

Recently, some scholars have explored the application of HEAs in the welding field. Bridges et al. [27] have successfully joined Inconel® 718 by laser brazing using

✉ Dejia Liu
ldj515@126.com
✉ Longzhi Zhao
zhaolongzhi@163.com
✉ Xiangjie Wang
415160823@qq.com

¹ School of Materials Science and Engineering, Economic and Technological Development Zone, East China Jiaotong University, Nanchang 330013, China

² Key Laboratory of Testing Technology for Manufacturing Process Ministry of Education, Southwest University of Science and Technology, Mianyang 621010, China

³ School of Mechanical and Electrical Engineering, Hubei Polytechnic University, Huangshi 435003, Hubei Province, China

a Ni–Mn–Fe–Co–Cu HEA filler metal. A maximum of 220 MPa shear strength was achieved in the brazed joint [27]. Zhang et al. [28] have designed a composite filler using FeCoNiCrCu HEA and pure Ti foil, which was used to braze ZrB₂–SiC–C ceramic and GH99 superalloy. A good bond between ZSC and GH99 was achieved, with the maximum shear strength of 71 MPa [28]. Voiculescu et al. [29] presented a welding deposition of FeCoCrNiAl HEA upon S275J2 steel by using tungsten inert gas welding. However, it should be pointed out that, designing the filler metal of HEA for brazing should consider the melting point and wetting properties, which may significantly restrict the element selection and reduce the mechanical properties of the brazed joints [27, 28]. Moreover, the fabricating process of the HEA-welding rod or wire would be complicated, which is not conducive to the early exploration of welding materials using HEAs. Laser deposition welding can easily change the compositions of the filler metal and is suitable for the design and optimization of high-entropy filler metals. Therefore, it is meaningful to explore the weld-ability of laser deposition welding by using filler metal based on a high-entropy design.

SMA490BW steel is a common material in the bogies of rail vehicles [30], which has good mechanical properties and corrosion resistance. However, sometimes SMA490BW steel is difficult to meet the service requirements of low temperature and humid environment. The 304 stainless steel, having high mechanical properties and strong corrosion resistance, would be an optional material used in the bogies [31]. Therefore, dissimilar welding of 304 stainless steel to SMA490BW steel has a practical application prospect in rail vehicles. In the present study, two kinds of multi-component mixed powders based on a high-entropy design are used as the filler metals, to achieve the dissimilar welding of 304 stainless steel to SMA490BW steel by laser deposition welding. Moreover, commercial 316L stainless steel powders are selected as comparative filler metal. By comparative analysis of the microstructure and mechanical properties of three types of dissimilar joints, the feasibility and weld-ability of the filler metals of multi-component mixed powders based on a high-entropy design were studied.

2 Experimental Procedures

The raw materials of iron, cobalt, chromium, nickel, manganese, and aluminum powders were used to manufacture the high-entropy filler metal in the experiment. The purity of those raw materials was more than 99.99 wt%. The granularity was 200–300 mesh. Multi-component mixed powders with a nominal Fe:Co:Cr:Ni:Mn molar ratio of 1:1:1:1:1 were used in this study, named as the FeCoCrNiMn powders. Another low-cost Co-free high-entropy filler metal was prepared by multi-component mixed powders with a nominal Cr:Fe:Ni:Al molar ratio of 1:1:2.4:0.6, named as the CrFeNi_{2.4}Al_{0.6} powders. Those powders were well-mixed by using a ball milling speed of 200 r/min and a ball milling time of 120 min. The ball material ratio of 3:1 was used. To evaluate the weld-ability of two types of high-entropy filler metal, commercial 316L stainless steel powders are selected as the comparative filler metal, named as 316L powders. Therefore, three types of filler metals were used in the study. The nominal element contents for three types of filler metal powders are presented in Table 1.

Commercial hot-rolled 304 stainless steel and SMA490BW steel (1.5 mm thick) were used as the initial materials, which were cut into 120 mm × 45 mm pieces. An LDM2500-60 semiconductor laser and K1000M4i-A numerical control system was used to carry out the laser deposition welding. Coaxial powder feeding and single focus welding were used during the welding process. A laser power of 1000 W, a scanning speed of 250 mm/min and a powder feeding amount of 15 g/min were used in this study. The laser spot size was approximately 1.5 mm. The gap between two base metals (BMs) for joining is about 0.7 mm in this study. A single-pass butt-welding between 304 stainless steel and SMA490BW steel was applied. The same technological parameters were used during the welding process for three types of filler metals.

After welding, the cross-section of the dissimilar joints vertical to welding direction (WD) was chosen for microstructure characterization. Optical microscopy (OM) and scanning electron microscopy (SEM) equipped with an energy-dispersive spectrum (EDS) were used to examine the microstructure and element distribution. Before the examination, metallographic specimens were ground and polished by standard methods. The SMA490BW steel was etched in a 4 vol% nitric acid-alcohol solution. The 304 stainless steel

Table 1 The nominal element contents for three types of filler metal powders (wt%)

Filler metal powders	Fe	Co	Cr	Ni	Mn	Al	Mo	Si
FeCoCrNiMn powders	19.92	21.02	18.54	20.93	19.59	-	-	-
CrFeNi _{2.4} Al _{0.6} powders	21.08	-	19.63	53.18	-	6.11	-	-
316L powders	Bal	-	16.79	10.66	0.2	-	2.42	1.0

was etched in an aqua regia solution. The weld zones (WZs) were etched in saturated ferric chloride solution and followed by 10 vol% nitric acid. Moreover, the phase constitution in three types of WZs was identified by X-ray diffraction (XRD) with Cu $K\alpha$ radiation. To avoid the BMs located in the measured surface, five sheets are cut and tightly glued together, and longitudinal sections of WZ were served as the measured surface. The diagram of sampling specimen for XRD test can be seen in Fig. 1a, b. And the shaded area in Fig. 1b was the measured surface for XRD test.

Microhardness distributions in three types of dissimilar joints were obtained with a 200 g load for a 10 s loading time by using an MH-3 Vickers microhardness tester. In order to accurately examine the tensile strength in the WZ, a standard notched tensile specimen was used in the present study. Considering the comparability of the tensile strength, the notched tensile specimens were employed for three types of dissimilar joints as well as two as-received plates. The sampling design and dimensions of those tensile specimens were shown in Fig. 1a, c. The transverse tensile test was performed at a strain rate of $1 \times 10^{-3} \text{ s}^{-1}$ at room temperature. SEM was used to examine the fracture surfaces as well as the microstructures near the fracture line.

To evaluate the corrosion resistance of the WZs by using three types of filler metals, potentiodynamic polarization tests were carried out in a corrosion cell containing 450 ml of 3.5-wt% NaCl solution at room temperature by using a corrosion measurement system. The measured specimens of the WZ are similar to the specimens using for XRD test (see Fig. 1b). Prior to the experiment, the measured surfaces were polished with 3000 grit emery paper to achieve a mirror finish. A three-electrode system was implemented: a saturated calomel electrode (SCE) and a platinum plate were used as the reference electrode, together with an auxiliary electrode. Potentiodynamic polarization tests were carried out at a scan speed of 0.5 mV/s and commencing from -1.8 V to -0.9 V . All potentials in the study are quoted with respect

to the SCE. Each test was repeated at least three times to obtain reliable results.

3 Results

3.1 Tensile Properties

Dissimilar metals of 304 stainless steel to SMA490BW steel are successfully joined by laser deposition welding by using three types of filler metal powders. A macroscopic view of the dissimilar joint welded by using the $\text{CrFeNi}_{2.4}\text{Al}_{0.6}$ powders is presented in Fig. 2. And the photographs of the cross-sections of various dissimilar joints of 304 stainless steel/SMA490BW steel are presented in Fig. 3. It is found that full penetration was achieved in three types of joints. Welding defects such as cracks and porosity are not observed in the joints. It means that, by using the filler metal powders based on a high-entropy design, a successful joining is achieved between the dissimilar metals of 304 stainless steel and SMA490BW steel. Moreover, the joint welded by

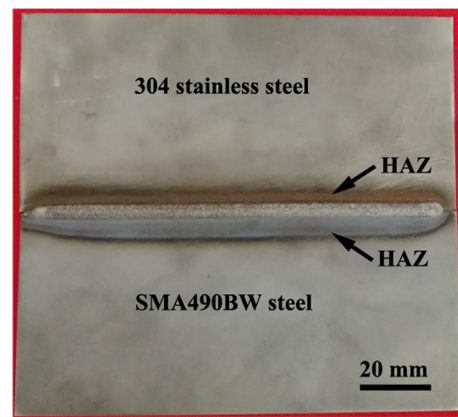
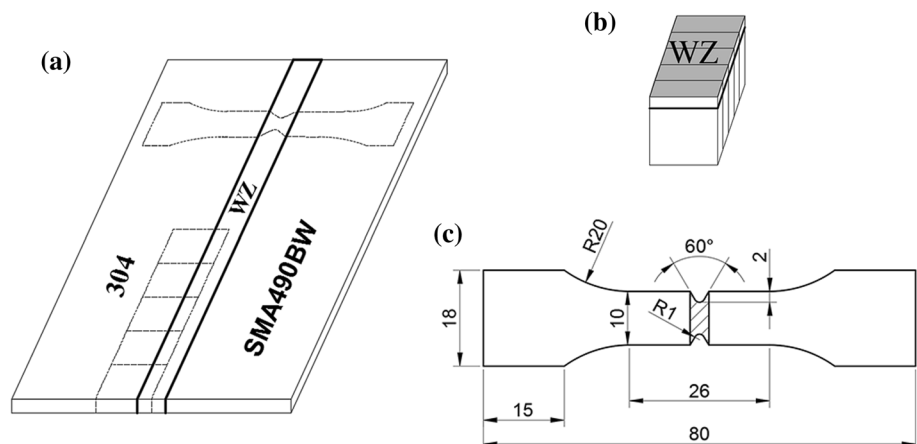


Fig. 2 Photograph of dissimilar joint of 304 stainless steel / SMA490BW steel welded using the powders of $\text{CrFeNi}_{2.4}\text{Al}_{0.6}$

Fig. 1 Sampling design of testing specimens for the dissimilar joints of 304 stainless steel / SMA490BW steel: **a** sampling location diagram; **b** the diagram of sampling specimen for XRD and potentiodynamic polarization tests; **c** the dimensions of notched tensile specimens (unit: mm)



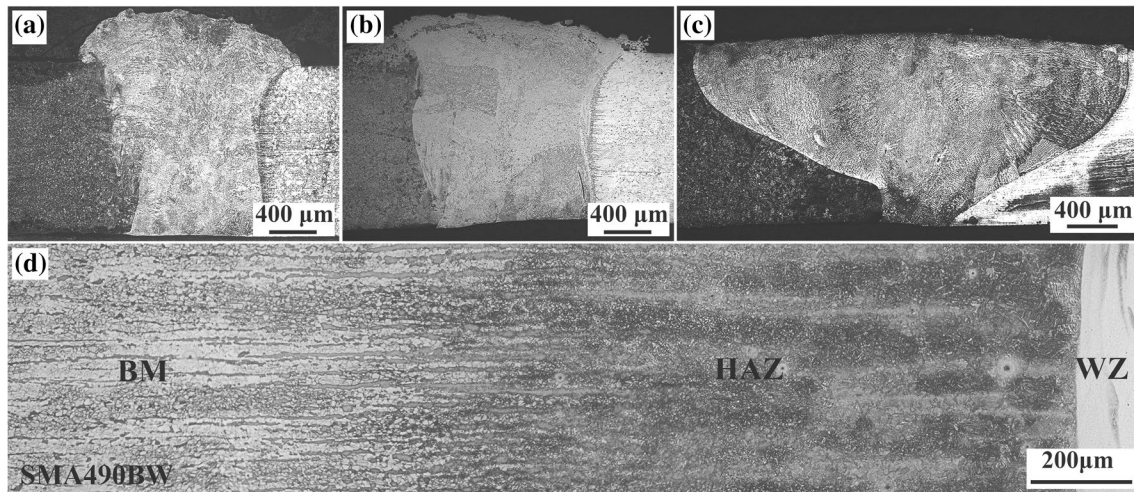


Fig. 3 Photographs (low-magnification) of the cross-sections of various dissimilar joints of 304 stainless steel/SMA490BW steel welded by using the powders of 316L (a) and FeCoCrNiMn (b) and

CrFeNi_{2.4}Al_{0.6} (c); **d** microstructure evolution from the BM to WZ in SMA490BW steel side for the joint welded by using the powders of FeCoCrNiMn

using the powders of CrFeNi_{2.4}Al_{0.6} presents a semi-circular morphology of the WZ (see Fig. 3c), which is largely different from the other two joints with a rectangular morphology (see Fig. 3a, b). The result is not a coincidence, which may be ascribed to the different compositions of three filler metals, especially for the presence of Al powders in the powders of CrFeNi_{2.4}Al_{0.6}. The width of the WZ is measured to be ~1.25 mm for the joint welded with the 316L powders, and that is ~1.51 mm for the joint welded with the FeCoCrNiMn powders. Microstructure evolution from the BM to WZ in SMA490BW steel side is showed in Fig. 3d. A wide heat affected zone (HAZ) is observed in SMA490BW steel side. The width of the HAZ is measured to be ~1.1 mm, which is slightly smaller than the WZ. The HAZ in SMA490BW steel side is much more obvious than that in 304 stainless steel side. The reason may be attributed to the larger thermal conductivity of SMA490BW steel compared to the 304 stainless steel. The different sizes of HAZ in two sides would have some effects on the mechanical properties of the dissimilar joints.

Notched tensile strengths are presented in Fig. 4a. The ultimate tensile strength (UTS) of the 304 stainless steel (~851 MPa) is much higher than that of the SMA490BW steel (~556 MPa). So the SMA490BW steel is considered as a “soft” material compared to the 304 stainless steel in this study. Figure 4a shows that the tensile strength of the joint by using the powders of FeCoCrNiMn (~859 MPa) is similar to that by using the powders of 316L (~875 MPa). The results are higher than that of the BM of SMA490BW steel and similar to the 304 stainless steel BM in this study. The lowest tensile strength among three types of dissimilar joints is found in the joint by using the powders of CrFeNi_{2.4}Al_{0.6}. The value is approximately 769 MPa, which

is lower than that of the 304 stainless steel and is higher than that of the SMA490BW steel. In addition, it should be stated that the UTS of the dissimilar joint using the powders of CrFeNi_{2.4}Al_{0.6} in this study, is similar to a HEA sample with a similar high-entropy component fabricated by vacuum arc melting reported in a recent study (~757 MPa) [12].

Macroscopic features of the fractured samples are presented in Fig. 4b. It is interesting that the fracture positions of three types of dissimilar joints are largely different. The dissimilar joint by using the powders of CrFeNi_{2.4}Al_{0.6} fractures in the WZ. The other two joints do not fracture at the notch of the tensile sample but fractured in the regions near the notch in the SMA490BW steel side. More detailed information about the fracture positions can be seen in the magnified view of the fracture areas in Fig. 4c–e. It is clear that the joints by using the powders of 316L and FeCoCrNiMn do not fracture in the WZ, but in SMA490BW steel side. It is measured that the fracture line is located in a distance of 0.32–1.79 mm from the BM/WZ interface in the SMA490BW steel side for the joint using the powders of 316L, and that is about 0.41–1.82 mm for the joint using the powders of FeCoCrNiMn. Based on the width of the HAZ (~1.1 mm) showed in Fig. 3d, the fracture mainly occurs in the HAZ as well as a small amount of BM in SMA490BW steel side. Figure 4c, d show severe necking existed in the SMA490BW steel BM for the fractured samples, with a distance of 1.79–1.82 mm from the BM/WZ interface. And the fracture lines are inclined ~45° to the TD in the HAZ. Therefore, it can be speculated that crack is initiated in the BM and near the HAZ in the middle of the specimen, and propagates toward the HAZ in SMA490BW steel side. The results indicate that the tensile strengths of those two types of WZs are higher than the BM of SMA490BW steel.

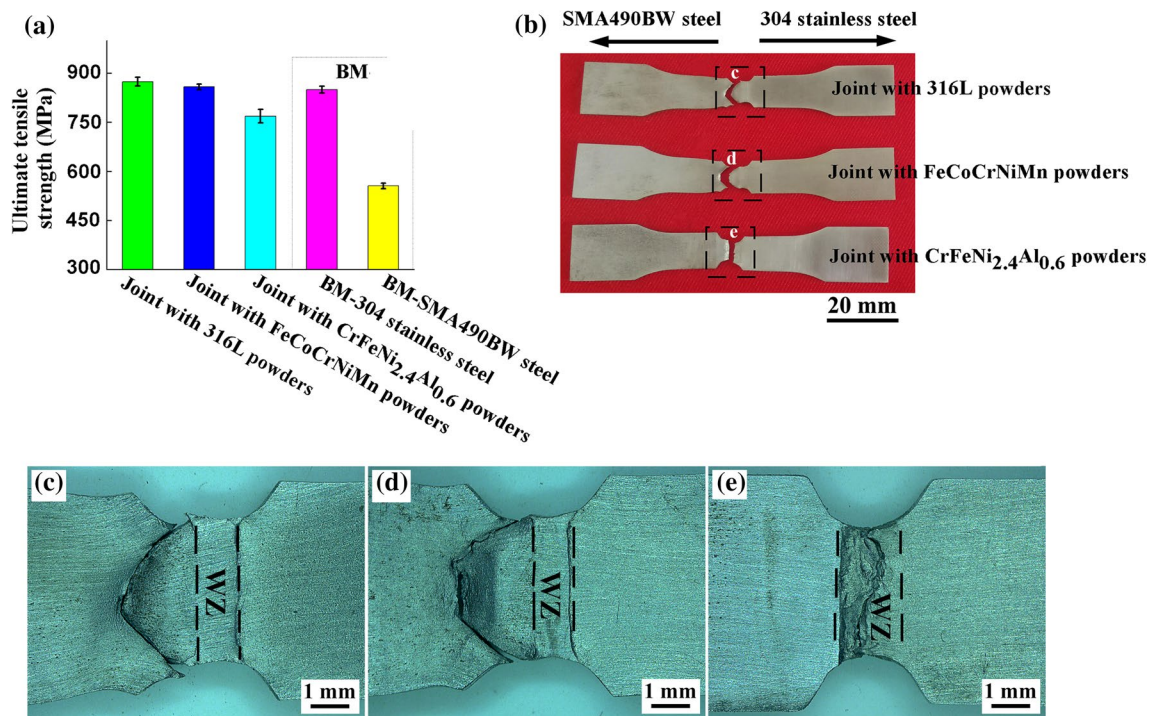
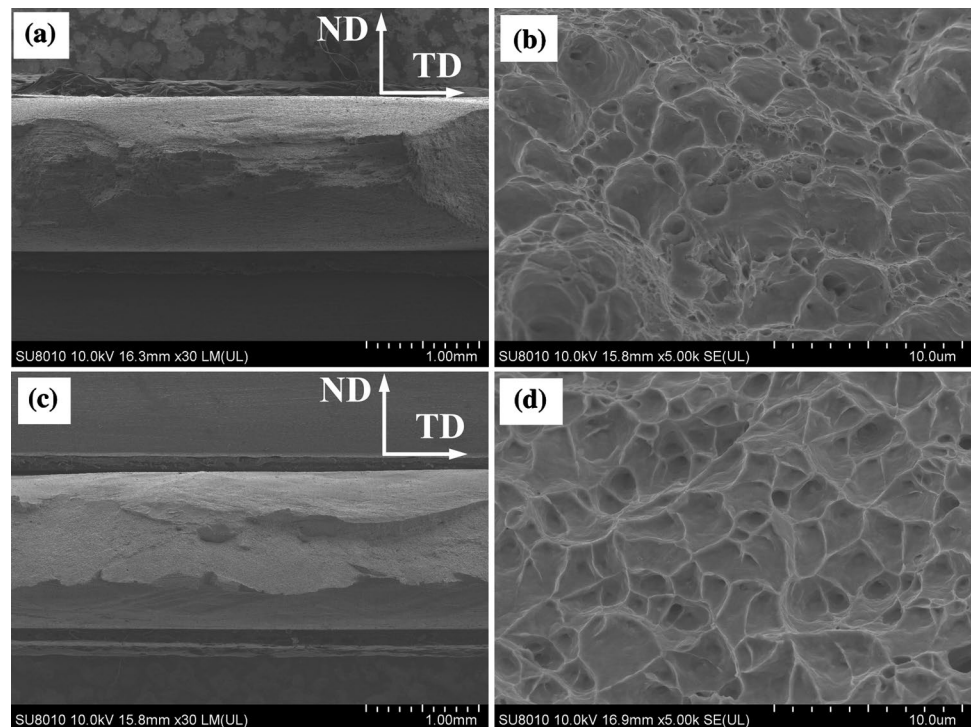


Fig. 4 Notched tensile strengths and fracture positions of the tensile test: **a** ultimate tensile strengths; **b** fracture positions. Magnified view of the fracture locations for the joints by using the powders of 316L (**c**) and FeCoCrNiMn (**d**) and CrFeNi_{2.4}Al_{0.6} (**e**)

Figure 5 present the SEM images of the fracture surfaces of the dissimilar joints of 304 stainless steel to SMA490BW steel. A typical dimple fracture was observed in both of the

fracture surfaces by using the powders of FeCoCrNiMn and CrFeNi_{2.4}Al_{0.6}. The formation of dimples indicates that both joints exhibit a ductile fracture mode. Moreover, the dimples

Fig. 5 Fracture surfaces of the dissimilar joints of 304 stainless steel/SMA490BW steel: **a, b** the joint welded with the powders of FeCoCrNiMn; **c, d** the joint welded with the powders of CrFeNi_{2.4}Al_{0.6}. *ND* Normal direction; *TD* Transverse direction



in the dissimilar joint by using the powders of $\text{CrFeNi}_{2.4}\text{Al}_{0.6}$ are finer than those in the dissimilar joint by using the powders of FeCoCrNiMn . The results may be related to the fracture positions and fracture behaviors of those two dissimilar joints.

To further study the fracture behavior of the dissimilar joints of 304 stainless steel to SMA490BW steel, the microstructures near the fracture line of the dissimilar joints were analyzed by SEM, and the results are presented in Fig. 6. A transgranular fracture occurs in both dissimilar joints by using the powders of FeCoCrNiMn and $\text{CrFeNi}_{2.4}\text{Al}_{0.6}$. Based on the magnified view of the fracture position presented in Fig. 4d, the joint by using the powders of FeCoCrNiMn fractured in the SMA490BW steel. Ferrite and pearlite are presented near the fracture line, which confirms that the fracture line is located in the SMA490BW steel. Because the microstructures of SMA490BW steel mainly consists of ferrite and pearlite [30]. Moreover, the fracture occurs in the ferrite region (see Fig. 6a), which may be attributed to the lower strength of the ferrite compared to the pearlite in the SMA490BW steel. Columnar crystals are observed near the fracture line of the dissimilar joint by using the powders of $\text{CrFeNi}_{2.4}\text{Al}_{0.6}$ (see Fig. 6b). Those columnar crystals may be the main reasons for the fine dimples in the fracture surface of this joint. As is known, columnar crystal usually shows lower plasticity compared to the equiaxed grains.

3.2 Hardness

The measured hardness profiles on the cross-section of three types of dissimilar joints are presented in Fig. 7. The hardness value in the BM of 304 stainless steel is approximately 200 HV, which is higher than that of the SMA490BW steel (~165 HV). Compared to the BM, a significant increase in hardness is observed in the HAZ of the SMA490BW steel side. The hardness value is approximately 300 HV. Figure 7 shows that the width of the HAZ is ~1 mm, which is well consistent with the results shown in Fig. 3d. However, a

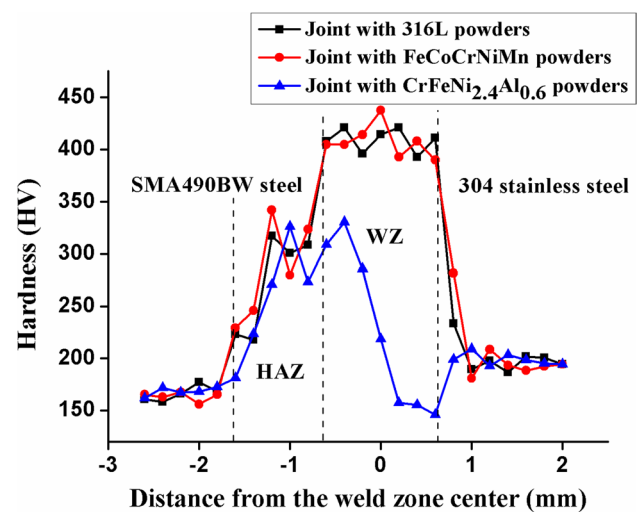


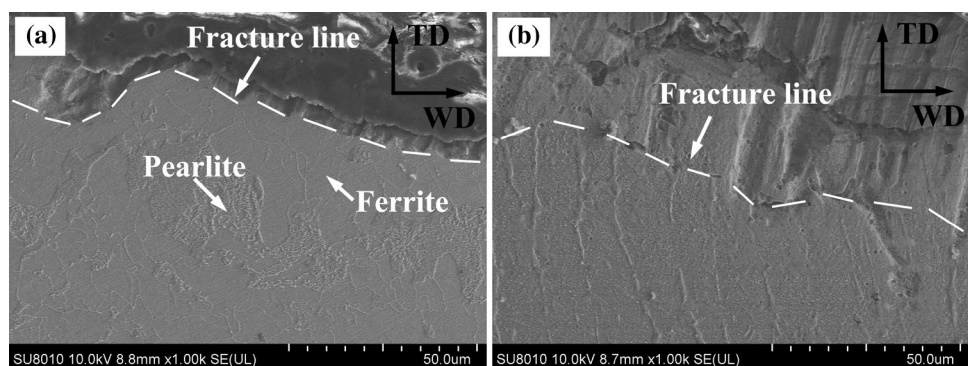
Fig. 7 Microhardness distributions in the transverse welds for various dissimilar joints of 304 stainless steel / SMA490BW steel

similar increase in hardness is not observed in the HAZ of the 304 stainless steel side (see Fig. 7).

Figure 7 shows that the hardness values in the WZ by using the powders of FeCoCrNiMn are similar to that by using the powders of 316L. Moreover, a small change of hardness value (~400 HV) is presented in those two types of WZs. And the hardness values are much higher than the BMs of 304 stainless steel and SMA490BW steel. The result confirms that the strength/hardness of those two types of WZs is higher than two types of BMs, which leads to those two dissimilar joints fractured in the SMA490BW steel, but not in the notch of the WZ (see Fig. 4c, d). It is noteworthy that the hardness value in the WZ by using the powders of FeCoCrNiMn in this study is higher than the FeCoCrNiMn HEAs reported in previous studies [32, 33].

Figure 7 presents that the hardness values in the WZ by using the powders of $\text{CrFeNi}_{2.4}\text{Al}_{0.6}$ are much lower than the other two joints. Moreover, a great variation of hardness value is observed in the WZ. The highest hardness value (~320 HV) in the WZ is presented near the fusion zone in

Fig. 6 Microstructures near the fracture line of the dissimilar joints of 304 stainless steel/ SMA490BW steel: **a** the joint welded using the powders of FeCoCrNiMn ; **b** the joint welded using the powders of $\text{CrFeNi}_{2.4}\text{Al}_{0.6}$. TD Transverse direction; WD Welding direction



SMA490BW steel side. The lowest hardness value (~ 140 HV) is presented near the fusion zone in 304 stainless steel side. The results are well consistent with the fracture position of the dissimilar joint welded by using the powders of $\text{CrFeNi}_{2.4}\text{Al}_{0.6}$. As described above, the dissimilar joint fractured in the WZ, slightly close to the 304 stainless steel side and columnar crystals are observed near the fracture line (see Fig. 6b).

3.3 Corrosion Resistance

Corrosion resistance is another index for the dissimilar joints of 304 stainless steel to SMA490BW steel. The results of potentiodynamic polarization tests are presented in Fig. 8. The corrosion current (I_{corr}) and corrosion potential (E_{corr}) values were measured, by considering the extensive linear region observed in the cathodic branch and a linear region in the anodic branch (Fig. 8). The results are presented in Table 2. The SMA490BW steel has the worst corrosion resistance with the lowest E_{corr} of -495.2 mV and the highest I_{corr} of 6.06×10^{-6} A/cm². The 304 stainless steel has a better corrosion resistance with the E_{corr} of -218.4 mV and

the I_{corr} of 1.44×10^{-7} A/cm² compared to the SMA490BW steel.

Large differences in E_{corr} and I_{corr} are observed among the three types of WZs (see Table 2). The dissimilar joint by using the powders of 316L presents the highest E_{corr} of -173.6 mV and an I_{corr} of 1.61×10^{-6} A/cm². The dissimilar joint by using the powders of $\text{CrFeNi}_{2.4}\text{Al}_{0.6}$ presents the lowest E_{corr} of -222.6 mV and an I_{corr} of 4.26×10^{-7} A/cm². The comparative E_{corr} and I_{corr} values of different specimens are observed in the following order: (a) E_{corr} : the joint by using 316L powders > the joint by using FeCoCrNiMn powders > the BM of 304 stainless steel > the joint by using $\text{CrFeNi}_{2.4}\text{Al}_{0.6}$ powders > the BM of SMA490BW steel, and (b) I_{corr} : the BM of 304 stainless steel < the joint by using FeCoCrNiMn powders < the joint by using $\text{CrFeNi}_{2.4}\text{Al}_{0.6}$ powders < the joint by using 316L powders < the BM of SMA490BW steel. The results indicate that all those WZs by using three types of filler metals have a better corrosion resistance than the BM of SMA490BW steel. It means that the corrosion resistance of those WZs by using the filler metals based on a high-entropy design can meet the service requirements.

3.4 Microstructure

Microstructures of two types of BMs are presented in Fig. 9a, b. Ferrite (in white color) and pearlite (in black color) are observed in the BM of SMA490BW steel (see Fig. 9a), while austenite is presented in the BM of 304 stainless steel (see Fig. 9b). Microstructures near the interfaces of BM and WZ in the dissimilar joints by using the powders of FeCoCrNiMn and $\text{CrFeNi}_{2.4}\text{Al}_{0.6}$ are presented in Fig. 9c–f. For both dissimilar joints, lath martensite is observed in the HAZ in the SMA490BW steel side (see Fig. 9c, e), which shows large differences compared to the BM of SMA490BW steel. The results are well consistent with the significant increase in hardness in the HAZ of the SMA490BW steel side (see Fig. 7). The results may be ascribed to the rapid cooling during the laser welding process. Similar martensite morphology is not observed in the HAZ of the 304 stainless steel side (see Fig. 9f). This may be ascribed to a high content of Ni element in the 304 stainless steel, which hinders the formation of martensite during the welding process.

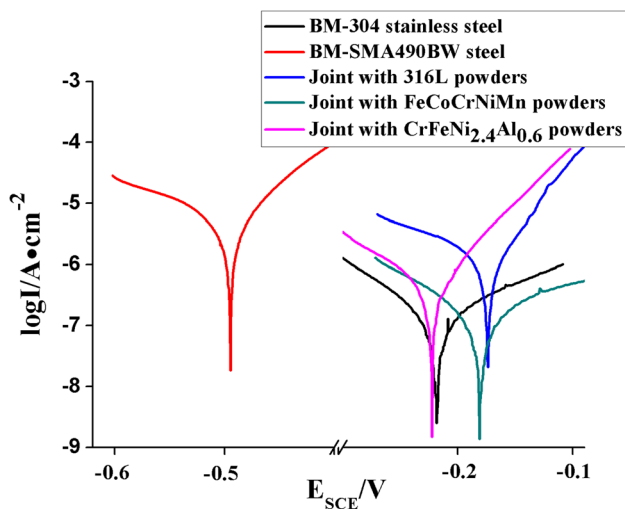
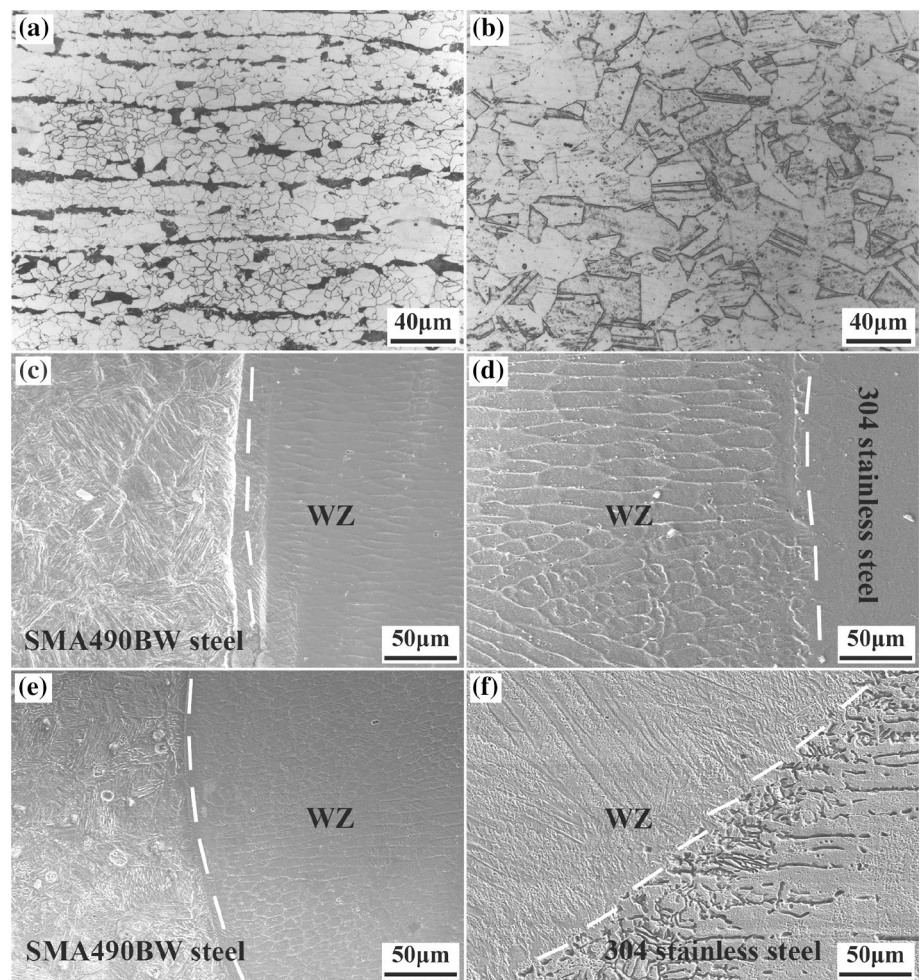


Fig. 8 Polarization curves of three types of dissimilar joints and the as-received plates in 3.5% NaCl solution

Table 2 Electrochemical parameter for different specimens in the potentiodynamic polarization tests

Specimens	Corrosion potential E_{corr} (mV vs. SCE)	Current density I_{corr} (A/cm ²)
Joint with the powders of 316L	-173.6	1.61×10^{-6}
Joint with the powders of FeCoCrNiMn	-181.1	1.53×10^{-7}
Joint with the powders of $\text{CrFeNi}_{2.4}\text{Al}_{0.6}$	-222.6	4.26×10^{-7}
The BM of 304 stainless steel	-218.4	1.44×10^{-7}
The BM of SMA490BW steel	-495.2	6.06×10^{-6}

Fig. 9 Microstructures of two BMs and the BM/WZ interfaces of in the dissimilar joints: **a** the BM of SMA490BW steel; **b** the BM of 304 stainless steel; **c, d** the joint welded using the powders of FeCoCrNiMn; **e, f** the joint welded using the powders of CrFeNi_{2.4}Al_{0.6}; **c, e** the interface in SMA490BW steel side; **d, f** the interface in 304 stainless steel side



Moreover, some streamline microstructures are presented near the fusion zone in the 304 stainless steel side (see Fig. 9f). An obvious orientation of the streamline microstructures is presented, which is spreading from the interface to the HAZ. Based on previous studies [31, 34], the streamline microstructures may be δ -ferrite. The formation of δ -ferrite would have a close relationship with the fast cooling rate during the laser deposition welding. The transformations between austenite and ferrite would occur in 304 stainless steel during heating and cooling in the welding process, especially in the regions near the fusion zones. However, the cooling rate during the laser welding is so fast, calculated to be 839 K/s [35], that there's not enough time for solute atoms in ferrite to occur a complete solid solution to form austenite, which results in some δ -ferrite existed near the fusion zones of the 304 stainless steel side. Previous studies reported that the formation of ferrite was possible when austenitic stainless steels heated to temperatures under solidus temperature [34, 35]. And the possibility of ferrite formation in HAZ is high in 304 stainless steel [35].

Elemental line scan of the BM/WZ interface in 304 stainless steel side was applied to analyze the elemental variation

near the interface. For the joints welded by using the powders of FeCoCrNiMn and CrFeNi_{2.4}Al_{0.6}, the measured positions are indicated as the white arrows provided in Fig. 10a, b. And the results are presented in Fig. 10c, d, respectively. Large differences in the atomic percentages of elements can be observed in two types of WZs near the BM/WZ interface in 304 stainless steel side (see Fig. 10c, d). Figure 10c shows that the main element in the WZ by using the powders of FeCoCrNiMn is Fe element. The atomic percentage of Fe element is fluctuating between 50 and 60. The atomic percentages of Co, Cr, Ni, and Mn elements are located in 7–17. The average measured atomic ratio of Fe:Co:Cr:Ni:Mn is about 54.1:12.1:17:7:9.8, for the WZ near the BM/WZ interface in 304 stainless steel side by using the powders of FeCoCrNiMn. However, for the WZ by using the powders of CrFeNi_{2.4}Al_{0.6}, Fe element also has the highest atomic percentage, which is fluctuating between 40 and 50. And the average measured atomic ratio of Fe:Cr:Ni:Al is about 45.2:31.1:16.6:7.1. The results indicate that the melting of BM and weld metal dilution during the welding process can significantly change the high-entropy component in the WZ.

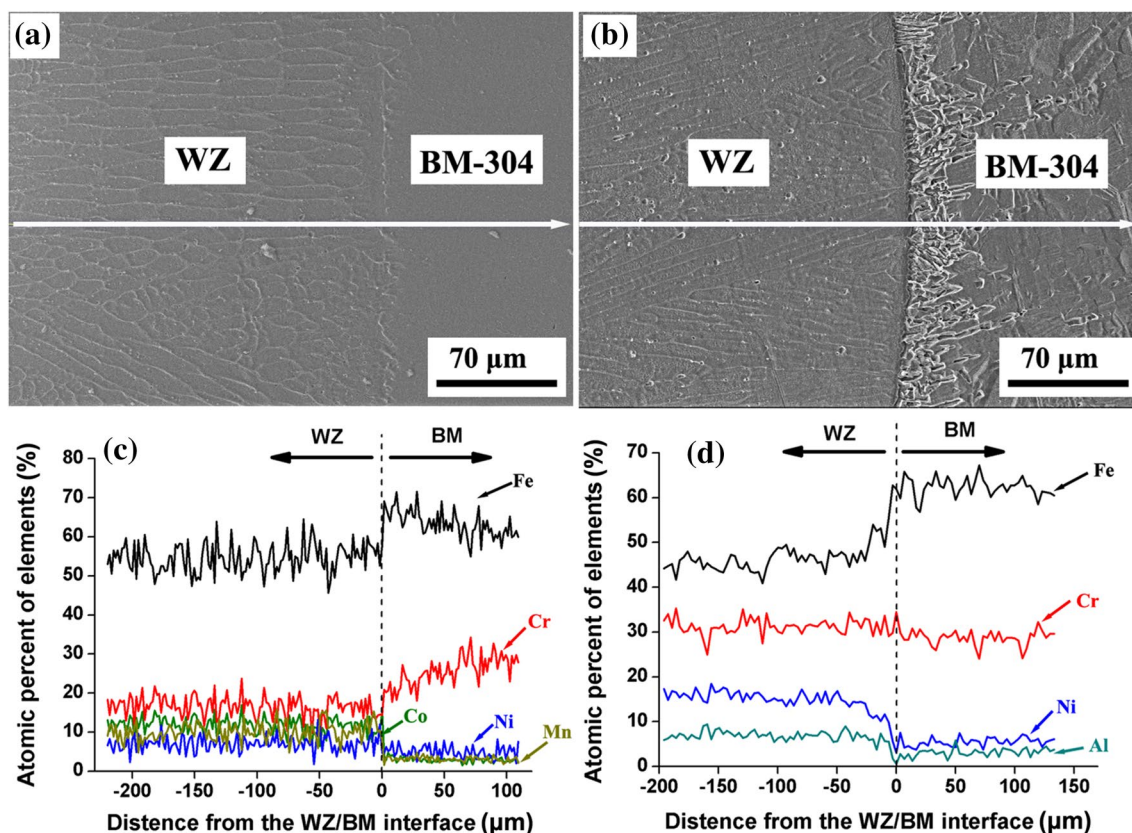


Fig. 10 Elemental line scan of the BM/WZ interface in 304 stainless steel side of the dissimilar joints: **a, c** the joint welded using the powders of FeCoCrNiMn; **b, d** the joint welded using the powders of CrFeNi_{2.4}Al_{0.6}

Microstructures in the WZs are presented in Fig. 11. Columnar crystals are presented in two sides of the WZs, and equiaxed grains are presented in the WZ-center. The low-magnification of microstructure evolution in the cross-section of WZ can be observed in Fig. 11a. Three typical regions in a WZ, including the regions near the fusion zones as well as the WZ center, are examined by SEM. The examined regions are indicated as the white dashed boxes showed in Fig. 11a. For the WZ by using the powders of FeCoCrNiMn, the average width of columnar crystals in two sides of the WZ is measured to be about 8.8 μm. Fine and uniform equiaxed grains are formed in the WZ center, with the average grain size of ~6.2 μm. XRD analysis of phases in those WZs is presented in Fig. 12. Face-centered cubic (FCC) and body-centered cubic (BCC) structures are formed in the WZs by using the powders of FeCoCrNiMn and 316L. However, based on previous studies [2, 25], only FCC structure would be obtained in FeCoCrNiMn HEA samples. Moreover, Fig. 10c indicates that the average atomic percentage of Fe element in the WZ is about 54.1, which is beyond the content of principal elements in HEA (being lower than 50%). Therefore, it is speculated that high-entropy structures may not be achieved in the WZ by using the powders of

FeCoCrNiMn. The reason may be attributed to the melting of BM and weld metal dilution, which causes a change of the set high-entropy component in the WZ.

For the WZ by using the powders of CrFeNi_{2.4}Al_{0.6}, columnar crystals are observed near the fusion zone in the 304 stainless steel side. However, the columnar crystals are less obvious in the SMA490BW steel side. The characteristics can be observed more clearly in Fig. 9e, f. Fine and uniform equiaxed grains, with the average size of ~11 μm, are formed in the WZ center (see Fig. 11f). Only a single FCC structure is formed in the WZ by using the powders of CrFeNi_{2.4}Al_{0.6} (see Fig. 12). Intermetallic compounds (Fe–Al or Ni–Al phases) are not observed in the WZ. Moreover, it should be pointed out that, the grain morphologies and phase structure in the WZ are similar to the Cr–Fe–Ni–Al HEA samples fabricated by vacuum arc melting [12]. Based on the results of elemental line scan, no element has more than 50 atomic percentages (see Fig. 10d). The results indicate that a high-entropy structure may be obtained in the WZ by using the powders of CrFeNi_{2.4}Al_{0.6}. It should be noted that the melting of BM and weld metal dilution are also presented in the welding process by using the powders of CrFeNi_{2.4}Al_{0.6}. However, the single-simple solid solution

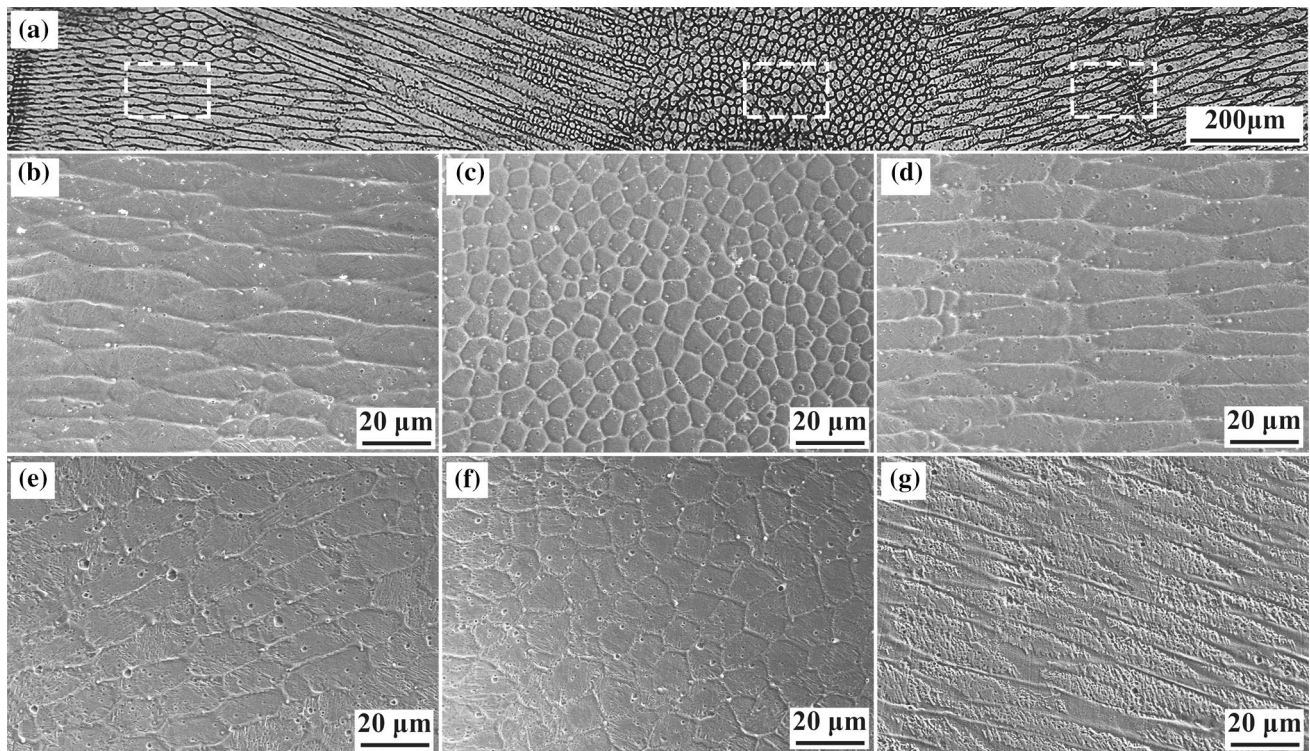


Fig. 11 Microstructures in the WZs by using the powders of FeCoCrNiMn and CrFeNi_{2.4}Al_{0.6}: **a** low-magnification of the cross-section of WZ; **b–d** the joint by using the powders of FeCoCrNiMn; **e–g** the

joint by using the powders of CrFeNi_{2.4}Al_{0.6}; **b, e** near the fusion zone in SMA490BW steel side; **c, f** WZ center; **d, g** near the fusion zone in 304 stainless steel side

phase, the most typical microstructure in HEAs, has not been changed by the weld metal dilution. The results indicate that the effect of weld metal dilution may be ignored, or reduced by selecting the appropriate components of filler metal powders with a high-entropy design, which will be further discussed in Sect. 4.

4 Discussion

Based on previous studies [3, 4, 11, 36], an excellent combination of high strength and good fracture toughness can be obtained in HEAs, which is particularly suitable for the application as the filler metal in welding. It should be noted that the chemical compositions and phase structures play a decisive role in the properties of HEAs [1, 2, 37]. How to control the chemical compositions in the WZ would be a key step in achieving high-entropy welded joints. In previous studies [27, 28], some HEAs were used as the filler metal during the braze welding. Owing to the un-melted BM in the braze welding, the limited element diffusion in the welding process has a small effect on the set high-entropy components in the WZ. However, the melting point of the filler metal should be lower than that of the BM, which would significantly restrict the element selection of HEA for braze welding. The high-entropy filler metals used for fusion welding can ignore the melting point, and have a wide range of element selection. However, based on the experimental results in the present study, the melting of BM and weld metal dilution during fusion welding may change the set high-entropy components in the WZ. Therefore, to achieve high-entropy welded joints, it is critical to control the compositions in the WZ.

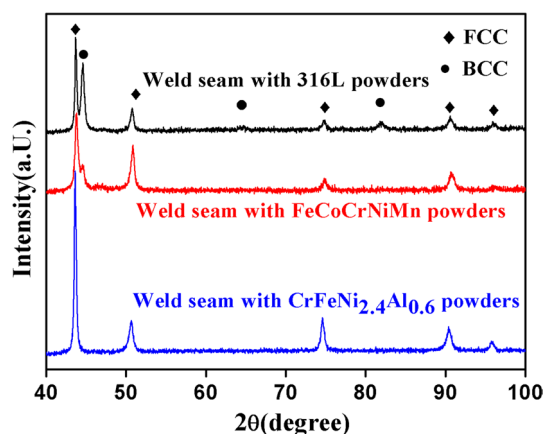


Fig. 12 XRD patterns of the welds for various dissimilar joints of 304 stainless steel / SMA490BW steel

As is known, the most fundamental and important feature regarding HEA is forming simple solid solution phases, and they can have outstanding properties [2, 36, 38]. Based on previous studies [39, 40], some physicochemical parameters, such as enthalpy of mixing (ΔH_{mix}), entropy of mixing (ΔS_{mix}), and atomic size differences (δ), have an impact on the phase formation in HEAs. The formula of those parameters can be seen as:

$$\bar{r} = \sum_{i=1}^n c_i r_i \quad (1)$$

$$\delta = \sqrt{\sum_{i=1}^n c_i \left[1 - \frac{r_i}{\bar{r}}\right]^2} \quad (2)$$

$$\Delta H_{mix} = \sum_{i=1}^n \Omega_{ij} c_i c_j \quad (3)$$

$$\Delta S_{mix} = -R \sum_{i=1}^n (c_i \ln c_i) \quad (4)$$

where c_i and c_j are the atomic percentages of an element in the alloy, r_i is the atomic radius of the element, \bar{r} is the average atomic radius, Ω_{ij} is four times of the binary alloy mixed enthalpy, and R is the molar gas constant (8.314 J/(K•mol)) [40]. Zhang et al. [41] and Guo et al. [42] reported that, to form sole simple phases (i.e. FCC, BCC) or their mixtures in HEAs, the following conditions have to be met simultaneously: $-22 \leq \Delta H_{mix} \leq 7$ kJ/mol, $\delta \leq 8.5$, and $11 \leq \Delta S_{mix} \leq 19.5$ J/(K mol) [42]. To form only simple ordered phase, the ranges of those parameters are more strict: $-15 \leq \Delta H_{mix} \leq 5$ kJ/mol, $\delta \leq 4.3$, and $12 \leq \Delta S_{mix} \leq 17.5$ J/(K mol) [41]

In order to analyze the effects of Fe element content on the phase structures in high-entropy welded joints, some physicochemical parameters of $\text{Fe}_x\text{CoCrNiMn}$ alloys are calculated to predict whether sole simple ordered phase or their mixtures can be formed in those alloys. Table 3 indicates that those physicochemical parameters of $\text{Fe}_x\text{CoCrNiMn}$ alloy ($1 \leq x \leq 2$) are located in the ranges of forming sole simple ordered phase, while $\text{Fe}_x\text{CoCrNiMn}$ alloys ($3 \leq x \leq 4$) are located in the ranges of forming multiphase structures. $\text{Fe}_x\text{CoCrNiMn}$ alloys ($x \geq 5$) are not located in the ranges of the criteria reported in previous studies [40, 41]. It means that the high-entropy structures may not be achieved in $\text{Fe}_x\text{CoCrNiMn}$ alloys ($x \geq 5$). The calculated results in Table 3 indicate that, as the content of Fe element increased to a certain amount, the phase structures in Fe–Co–Cr–Ni–Mn alloys would become more complicated. Moreover, the high entropy effect may disappear in those alloys. In fact, according to the gap between two BMs for joining as well as the cross-sections of WZs presented in Fig. 3, the weld metal dilution can be calculated by the area ratio of the melted BMs to the WZ in cross-section. It is measured that the weld metal dilution is about 38.1% for the WZ by using the powders of FeCoCrNiMn . The large weld metal dilution in the study can significantly increase the content of Fe element in the WZ, which leads to the actual atomic ratio of Fe:Co:Cr:Ni:Mn being about 54.1:12.1:17:7:9.8, for the WZ regions near the fusion zone in 304 stainless steel sides (see Fig. 10c). The calculated physicochemical parameters of $\text{Fe}_{54.1}\text{Co}_{12.1}\text{Cr}_{17}\text{Ni}_7\text{Mn}_{9.8}$ are provided in Table 3. It can be found that the value of ΔS_{mix} is calculated to be 10.8 J/(K mol), which is not located in the ranges of the criteria. It may confirm that high-entropy

Table 3 Calculated physicochemical parameters in $\text{Fe}_x\text{CoCrNiMn}$ and $\text{CrFe}_x\text{Ni}_{2.4}\text{Al}_{0.6}$ alloys

Alloy	δ (%)	ΔH_{mix} (KJ/mol)	ΔS_{mix} (J/(K mol))	T_{mix} (K)	Ω	Results
FeCoCrNiMn	4.03	- 4.16	13.38	1801.2	5.79	Sole simple ordered phase
$\text{Fe}_2\text{CoCrNiMn}$	3.09	- 3.37	12.98	1802.8	6.94	Sole simple ordered phase
$\text{Fe}_3\text{CoCrNiMn}$	2.93	- 2.78	12.26	1804.0	8.03	Multiphase structure
$\text{Fe}_4\text{CoCrNiMn}$	2.79	- 2.38	11.53	1804.9	8.76	Multiphase structure
$\text{Fe}_5\text{CoCrNiMn}$	2.67	- 2.05	10.83	1805.6	9.54	/
$\text{Fe}_6\text{CoCrNiMn}$	2.56	- 1.84	10.21	1806.1	10.01	/
$\text{CrFeNi}_{2.4}\text{Al}_{0.6}$	4.60	- 10.63	10.40	1739.6	1.70	/
$\text{CrFe}_2\text{Ni}_{2.4}\text{Al}_{0.6}$	4.37	- 8.79	10.49	1751.5	2.90	/
$\text{CrFe}_3\text{Ni}_{2.4}\text{Al}_{0.6}$	4.12	- 6.41	10.13	1760.0	2.78	/
$\text{CrFe}_4\text{Ni}_{2.4}\text{Al}_{0.6}$	3.90	- 6.51	9.66	1766.4	2.62	/
$\text{CrFe}_5\text{Ni}_{2.4}\text{Al}_{0.6}$	3.70	- 5.75	9.17	1771.3	2.82	/
$\text{CrFe}_6\text{Ni}_{2.4}\text{Al}_{0.6}$	3.57	- 5.16	8.71	1775.3	3.00	/
$\text{Fe}_{54.1}\text{Co}_{12.1}\text{Cr}_{17}\text{Ni}_7\text{Mn}_{9.8}$	2.53	- 1.89	10.8	1838.7	10.51	
$\text{Cr}_{31.1}\text{Fe}_{45.2}\text{Ni}_{16.6}\text{Al}_{7.1}$	5.03	- 8.05	10.6	1793.7	2.37	/

structures are not achieved in the WZ by using the powders of FeCoCrNiMn.

For CrFeNi_{2.4}Al_{0.6} alloy, the value of ΔS_{mix} is calculated to be 10.4 J/(K mol), which is not located in the ranges of forming sole simple phases (i.e. FCC, BCC) or their mixtures based on the criteria in previous studies [40, 41]. And the value of ΔS_{mix} in the CrFe_xNi_{2.4}Al_{0.6} alloy was decreased as the content of Fe element was increased, which is far away from the range of 12–17.5 J/(K mol). Based on the measured atomic ratio of Fe: Cr: Ni: Al in the regions near the fusion zone in 304 stainless steel sides (see Fig. 10d), the calculated physicochemical parameters of Cr_{31.1}Fe_{45.2}Ni_{16.6}Al_{7.1} (see Table 3) are not located in the ranges of the criteria reported in previous studies [40, 41]. However, it should be pointed out that, based on a previous study [12], CrFeNi₂Al alloy is a eutectic HEA system, even if the physicochemical parameters are not located in the ranges of the criteria. And CrFeNi_{2.4}Al_{0.6} alloy was confirmed to be a complete solid solution, and with a single FCC phase [12]. The results mean that some errors may occur in the prediction of phase structures in high-entropy welded joints based on the criterions mentioned above.

There are some other criterions to predict the phase structures in HEAs, such as the parameter of $\Omega = \frac{T_{mix}\Delta S_{mix}}{|\Delta H_{mix}|}$ [40]. It was reported that $\Omega \geq 1.1$ and $\delta < 6.6\%$ are the criteria for forming single solid solutions in HEAs [39, 43]. And Fe_xCoCrNiMn and CrFe_xNi_{2.4}Al_{0.6} alloys ($1 \leq x \leq 6$), as well as Fe_{54.1}Co_{12.1}Cr₁₇Ni₇Mn_{9.8} and Cr_{31.1}Fe_{45.2}Ni_{16.6}Al_{7.1} are all located in the ranges of $\Omega \geq 1.1$ and $\delta < 6.6\%$. It means that a complete solid solution could be formed in those multi-component alloys, even if the content of Fe element was increased to a large value (being larger than 50 at%). The prediction is clearly inconsistent with the actual results in iron-based alloys [44]. Tsai et al. [40] suggested that, even if an alloy is designed following these criterions, it can still contain intermetallic phases. According to the map of the superimposed effect of ΔH_{mix} , ΔS_{mix} , and δ on phase stability in multicomponent alloys, the ‘solid solution’ region still contains intermetallic phases [40]. Therefore, the prediction of phase structures in high-entropy welded joints based on the current criterions would be incorrect in sometimes. In addition, it should be pointed out that, the criterions of the phase formation in HEAs reported in previous studies [41, 42], are established in a relatively stable solidification environment, such as vacuum arc melting, etc. There would be a large error as it was used in the welding environment with a rapid heating and cooling rate.

As stated above, a high-entropy structure may not be achieved in the WZ by using the powders of FeCoCrNiMn. But it may be obtained in the WZ by using the powders of CrFeNi_{2.4}Al_{0.6}. The reasons may have some relationship with the type and content of elements in the high-entropy

filler metals as well as the phase identification in the WZs. According to the valence electron concentration (VEC) rules and previous studies [1, 2, 12], more Fe element increases the formation of BCC phase, while more Ni element promotes the formation of FCC phase in HEA samples. The weld metal dilution significantly increases the content of Fe element, and results in ~54.1 at% of Fe element for the WZ near the BM/WZ interface in 304 stainless steel side by using the powders of FeCoCrNiMn (see Fig. 10c). The increase in the content of Fe element promotes the formation of BCC phase and causes FCC and BCC structures observed in the WZ by using the powders of FeCoCrNiMn (see Fig. 12). The results are dissimilar to the phase structures in FeCoCrNiMn HEA samples reported in previous studies [2, 25]. Moreover, the large content of Fe element in the WZ (~54.1 at%) is beyond the content of principal elements in HEA. Therefore, high-entropy structures may not be achieved in the WZ by using the powders of FeCoCrNiMn.

However, for the WZ by using the powders of CrFeNi_{2.4}Al_{0.6}, owing to the large content of nickel powders in the multi-component mixed powders, the content of Ni element in the WZ (~16.6 at%) is much higher than that in the WZ by using the powders of FeCoCrNiMn (~7 at%). And the content of Fe element (~45.2 at%) is lower than that of the latter (~54.1 at%) (see Fig. 10). The more Ni element and less Fe element promote a single FCC structure formed in the WZ by using the powders of CrFeNi_{2.4}Al_{0.6} (see Fig. 12). The phase structure and grain morphologies in the WZ are similar to the Cr–Fe–Ni–Al HEA samples reported in the previous study [12]. And no element has more than 50 atomic percentages in the WZ. Therefore, it is concluded that high-entropy structures may be obtained in the WZ by using the powders of CrFeNi_{2.4}Al_{0.6}. As a summary, in the present study, the multi-component mixed powders of FeCoCrNiMn and CrFeNi_{2.4}Al_{0.6}, based on a high-entropy design, were used to achieve the dissimilar welding of 304 stainless steel to SMA490BW steel by laser deposition welding. And the feasibility and weld-ability of the filler metal powders based on a high-entropy design were studied by the comparative analysis of the microstructure and mechanical properties of those dissimilar joints.

5 Conclusions

- (1) Multi-component mixed powders of FeCoCrNiMn and CrFeNi_{2.4}Al_{0.6}, based on a high-entropy design, were successfully used as the filler metals to join the dissimilar metals of 304 stainless steel to SMA490BW steel by laser deposition welding.
- (2) The melting of BM and weld metal dilution during the laser deposition welding had an impact on the set high-entropy component in the WZ. High-entropy struc-

tures were achieved in the WZ by using the powders of $\text{CrFeNi}_{2.4}\text{Al}_{0.6}$.

- (3) All the dissimilar joints welded with three types of filler metals presented a higher notched tensile strength compared to the BM of SMA490BW steel. And all those WZs had a better corrosion resistance than the BM of SMA490BW steel.
- (4) The dissimilar joint welded using the powders of $\text{CrFeNi}_{2.4}\text{Al}_{0.6}$ had the lowest hardness value in the WZ, in which the joint was fractured during the notched tensile tests. The other two joints fractured at the regions near the notch in the SMA490BW steel side. Transgranular fracture and a typical dimple fracture were observed in the fractured joints.

Acknowledgements This study was financially supported by National Natural Science Foundation of China (51805171), Natural Science Foundation in Jiangxi Province (20181BAB216021), the Opening Project of Key Laboratory of Testing Technology for Manufacturing Process (Southwest University of Science and Technology), Ministry of Education (18kfkz04), Jiangxi Provincial Department of Education (GJJ180347).

Compliance with ethical standards

Conflict of interest The authors declare that they have no conflict of interest.

References

1. Y. Zhang, T.T. Zuo, Z. Tang, M.C. Gao, K.A. Dahmen, P.K. Liaw, Z.P. Lu, *Prog. Mater. Sci.* **61**, 1 (2014)
2. D.B. Miracle, O.N. Senkov, *Acta Mater.* **122**, 448 (2017)
3. B. Gludovatz, A. Hohenwarter, D. Catoor, E.H. Chang, E.P. George, R.O. Ritchie, *Science* **345**, 1153 (2014)
4. Z. Li, K.G. Pradeep, Y. Deng, D. Raabe, C.C. Tasan, *Nature* **534**, 227 (2016)
5. K. Tazuddin, N.P. Biswas, Gurao. *Mat. Sci. Eng. A* **657**, 224 (2016)
6. R. Li, M. Wang, T. Yuan, B. Song, Y. Shi, *Metall. Mater. Trans. A* **48**, 841 (2016)
7. Z. Wu, C.M. Parish, H.J. Bei, *J. Alloy. Compd.* **647**, 815 (2015)
8. G.D. Sathiaraj, P.P. Bhattacharjee, *J. Alloy. Compd.* **647**, 82 (2015)
9. Ł. Rogal, Z. Szklarz, P. Bobrowski, D. Kalita, G. Garzeń, A. Tarasek, M. Kot, M. Szczyngier, *Met. Mater. Int* (2019). <https://doi.org/10.1007/s12540-018-00236-5>
10. X. Qiu, *J. Alloy. Compd.* **735**, 359 (2018)
11. J. Joseph, N. Stanford, P. Hodgson, D.M. Fabijanic, *J. Alloy. Compd.* **726**, 885 (2017)
12. X. Jin, J. Bi, L. Zhang, Y. Zhou, X. Du, Y. Liang, B. Li, *J. Alloy. Compd.* **770**, 655 (2019)
13. H. Nam, C. Park, J. Moon, Y. Na, H. Kim, N. Kang, *Mat. Sci. Eng. A* **742**, 224 (2019)
14. Z.G. Zhu, F.L. Ng, J.W. Qiao, P.K. Liaw, H.C. Chen, S.M.L. Nai, J. Wei, G.J. Bi, *Mater. Res. Express* **6**, 046514 (2019)
15. R. Sokkalingam, K. Sivaprasad, V. Muthupandi, M. Duraiselvam, *Key Eng. Mater.* **775**, 448 (2018)
16. N. KashaeV, V. Ventzke, N. Stepanov, D. Shaysultanov, V. Sanin, S. Zharebtsov, *Intermetallics* **96**, 63 (2018)
17. N. Xu, Q. Song, Y. Bao, *Mater. Sci. Technol.* **35**, 577 (2019)
18. Z.G. Zhu, Y.F. Sun, F.L. Ng, M.H. Goh, P.K. Liaw, H. Fujii, Q.B. Nguyen, Y. Xu, C.H. Shek, S.M.L. Nai, J. Wei, *Mater. Sci. Eng. A* **711**, 524 (2018)
19. D. Shaysultanov, N. Stepanov, S. Malopheyev, I. Vysotskiy, V. Sanin, S. Mironov, R. Kaibyshev, G. Salishchev, S. Zharebtsov, *Mater. Charact.* **145**, 353 (2018)
20. Z.G. Zhu, Y.F. Sun, M.H. Goh, F.L. Ng, Q.B. Nguyen, H. Fujii, S.M.L. Nai, J. Wei, C.H. Shek, *Mater. Lett.* **205**, 142 (2017)
21. M.-G. Jo, H.-J. Kim, M. Kang, P.P. Madakashira, E.S. Park, J.-Y. Suh, D.-I. Kim, S.-T. Hong, H.N. Han, *Met. Mater. Int.* **24**, 73 (2018)
22. A.C. Martin, C. Fink, *Weld. World* (2019). <https://doi.org/10.1007/s40194-019-00702-7>
23. Z. Wu, S.A. David, D.N. Leonard, Z. Feng, H. Bei, *Sci. Technol. Weld. Join.* (2018). <https://doi.org/10.1080/13621718.2018.1430114>
24. R. Sokkalingam, S. Mishra, S.R. Cheethirala, V. Muthupandi, K. Sivaprasad, *Metall. Mater. Trans. A* **48**, 3630 (2017)
25. Z. Wu, S.A. David, Z. Feng, H. Bei, *Scripta Mater.* **124**, 81 (2016)
26. H. Nam, C. Park, C. Kim, H. Kim, N. Kang, *Sci. Technol. Weld. Joi.* **23**, 420 (2017)
27. D. Bridges, S. Zhang, S. Lang, M. Gao, Z. Yu, Z. Feng, A. Hu, *Mater. Lett.* **215**, 11 (2018)
28. L.X. Zhang, J.M. Shi, H.W. Li, X.Y. Tian, J.C. Feng, *Mater. Des.* **97**, 230 (2016)
29. I. Voiculescu, V. Geanta, I.M. Vasile, R. Stefanoiu, M. Tonoiu, *J. Optoelectron. Adv. Mater.* **15**, 650 (2013)
30. Y. Liu, N. Xi, S. Fu, G. Yang, H. Fu, H. Chen, X. Zhang, N. Liu, W. Gao, *Mater. Res. Express* **5**, 115030 (2018)
31. H. Ma, G. Qin, P. Geng, F. Li, B. Fu, X. Meng, *Mater. Des.* **86**, 587 (2015)
32. H. Cheng, Y.-C. Xie, Q.-H. Tang, C. Rao, P.-Q. Dai, T. Nonferr, *Metal. Soc.* **28**, 1360 (2018)
33. W.H. Liu, Y. Wu, J.Y. He, T.G. Nieh, Z.P. Lu, *Scr. Mater.* **68**, 526 (2013)
34. X. Shi, K. Yu, L. Jiang, C. Li, Z. Li, X. Zhou, *Surf. Coat. Tech.* **334**, 19 (2018)
35. H.M. Soltani, M. Tayebi, *J. Alloy. Comp.* **767**, 112 (2018)
36. J.H. Kim, Y.S. Na, *Met. Mater. Int.* **25**, 296 (2018)
37. J.W. Won, M. Kang, H.-J. Kwon, K.R. Lim, S.M. Seo, Y.S. Na, *Met. Mater. Int.* **24**, 1432 (2018)
38. M.J. Jang, S.-H. Joo, C.-W. Tsai, J.-W. Yeh, H.S. Kim, *Met. Mater. Int.* **22**, 982 (2016)
39. J.-X. Fu, C.-M. Cao, W. Tong, L.-M. Peng, *Trans. Nonferr. Metal. Soc.* **28**, 931 (2018)
40. M.-H. Tsai, J.-W. Yeh, *Mater. Res. Lett.* **2**, 107 (2014)
41. Y. Zhang, Y.J. Zhou, J.P. Lin, G.L. Chen, P.K. Liaw, *Adv. Eng. Mater.* **10**, 534 (2008)
42. S. Guo, C.T. Liu, *Prog. Nat. Sci. -Mater.* **21**, 433 (2011)
43. X. Yang, Y. Zhang, *Mater. Chem. Phys.* **132**, 233 (2012)
44. G. Bonny, C. Domain, N. Castin, P. Olsson, L. Malerba, *Comp. Mater. Sci.* **161**, 309 (2019)

Publisher's Note Springer Nature remains neutral with regard to jurisdictional claims in published maps and institutional affiliations.